Assessment of Suomi National Polar-Orbiting Partnership VIIRS Emissive Band Calibration and Inter-Sensor Comparisons

Quanhua Liu, Changyong Cao, and Fuzhong Weng

***Abstract*—Visible-Infrared Imager-Radiometer Suite (VIIRS), Moderate-resolution Imaging Spectroradiometer (MODIS), and Advanced Very High Resolution Radiometer (AVHRR) have similar thermal emissive bands and are used to determine surface temperature, fire product, and cloud properties. The Suomi National Polar-orbiting Partnership Cross-track Infrared Sounder (CrIS) is a hyperspectral sensor covering the most infrared spectrum. This study focuses on VIIRS sensor performance in which inter-sensor comparisons are crucial to the sensor's verification and validation. VIIRS thermal emissive bands (TEB) calibration data (blackbody and space counts) have been analyzed. The analysis results indicate that VIIRS TEB is stable. VIIRS Blackbody temperature is stable, too. The six platinum resistance thermometers (PRTs) are also stable, except for the third and sixth PRTs have a periodic variation of 50 mK. Using the calibration data during the Blackbody temperature cool down and warm up, we found that noise equivalent deviation of temperatures (NeDT) varies with the Blackbody temperature. We developed a model that can predict the scene temperature dependent NeDT for the VIIRS M15 band. Comparisons between the VIIRS and other sensors such as AVHRR, MODIS and CrIS demonstrated that VIIRS TEB agrees generally with those sensors within 0.5 Kelvin. It was found that azimuth angle difference between two detectors for the same scan can be very large, causing VIIRS image striping.**

***Index Terms*—CrIS, inter-sensor calibration, MODIS, thermal emissive band, VIIRS.**

I. Introduction

THE successful launch of the Suomi National Polar-orbiting Partnership (NPP) Spacecraft on Oct. 28, 2011 with the Visible Infrared Imaging Radiometer Suite (VIIRS) starts a new generation of capabilities for operational environmental remote sensing for weather, climate, ocean, and other environmental applications. VIIRS was turned on 8th November, 2011 for measuring reflective band radiance. The VIIRS Cryo-cooler door was opened on 18th January 2012, starting the observations for thermal emissive bands.

VIIRS succeeds the National Oceanic and Atmospheric Administration (NOAA) AVHRR, National Aeronautics and Space Administration (NASA) Earth Observation System (EOS) MODIS, and Defense Meteorological Satellite Program (DMSP) Operational Linescan System (OLS) with 22 spectral bands covering wavelengths from 0.41 to 12.5 μm [1], providing data for the production of 24 Environmental Data Records (EDRs) with its calibrated and geolocated Sensor Data Record (SDRs). Table I summarizes the VIIRS sensor characteristics and VIIRS related environmental data records (EDRs).

VIIRS significantly outperforms the legacy of current operational sensor AVHRR [2] in spatial, spectral, and radiometric areas by design [3]. The VIIRS has a wide swath of 3000 km. The 22 spectral bands in the visible, near-infrared, mid-infrared, and long-wave infrared regions of the electromagnetic spectrum are acquired at two spatial resolutions: 0.375 km for imagery (I) bands, and 0.75 km for moderate (M) resolution radiometry bands at nadir. Using a pixel aggregation strategy and manages data compression with several strategies including the so-called "bow-tie" removal, the VIIRS achieves a resolution of 0.8 km for imagery bands, and 1.6 km for moderate resolution radiometry bands at the edge of scan [4]. Fig. 1 illustrates the VIIRS M band pixel size variation with the scan angle of the VIIRS. For the VIIRS M band, the original pixel size is 0.742 km in track direction and 0.259 km in scan direction. Three aggregation zones are selected. In zone I for the scan angles between 0° and 31.59°, 3 pixels are aggregated in the scan direction. In zone II for the scan angles between 31.59° and 44.68°, 2 pixels are aggregated in the scan direction. In the zone III for the scan angles between 44.68° and 56.06 °, no aggregation is applied.

VIIRS Day Night Band (DNB) has a unique capability for night time environmental applications with 0.75 km spatial resolution. After subtracting background noise, the VIIRS DNB shows a beautiful image of cities' light and moon light reflected by clouds. More information about VIIRS can be found at the following VIIRS websites: http://www.star.nesdis.noaa.gov/jpss/VIIRS.php, and https://cs.star.nesdis.noaa.gov/NCC/VIIRS, where users can find the relative spectral response data, user's guide, algorithm theoretical basis documents (ATBD), instrument performance data on-orbit, sample codes to read the VIIRS SDR data, conference presentations, and image gallery, etc..

The VIIRS SDR contains radiometric calibration and geolocation. The VIIRS geolocation is excellent with an accuracy better than 80 meters in both scan and along track directions. This study focuses on radiometric calibration and assessment only. The VIIRS radiometric calibration concept is common:

Manuscript received September 28, 2012; revised March 28, 2013 and May 06, 2013; accepted May 09, 2013. Date of current version June 17, 2013. This work was supported by JPSS Data Products and Algorithms and the Joint Center for Satellite Radiance Assimilation.

Q. Liu is with ESSIC, University of Maryland, College Park, MD 20740-3822 USA. He is also with the Joint Center for Satellite Data Assimilation, College Park, MD 20740-3822 USA.

C. Cao and F. Weng are with the NOAA/NESDIS/STAR/Satellite Meteorology and Climatology Division, College Park, MD 20740-3822 USA.

Digital Object Identifier 10.1109/JSTARS.2013.2263197

1939-1404/$31.00 © 2013 IEEE

TABLE I
VIIRS SENSOR SPECIFICATION, PRELAUNCH ASSESSMENT, AND RELEVANT APPLICATIONS

				Specification							Prelunch
		Band No.	Driving EDR(s)	Spectral Range (um)	Horiz Sample Interval (km) (track x Scan)		Band Gain	Ltyp or Ttyp (Spec)	Lmax or Tmax	Spec SNR or NEdT (K)	Measured SNR or NEdT (K)
					Nadir	End of Scan					
Reflective Bands	VisNIR	M1	Ocean Color Aerosol	0.400 - 0.420	0.742 - 0.259	1.60 x 1.58	High	44.9	135	352	616.8
							Low	155	615	316	1092
		M2	Ocean Color Aerosol	0.435 - 0.450	0.742 - 0.259	1.60 x 1.58	High	40	127	380	622.4
							Low	146	687	409	1118
		M3	Ocean Color Aerosol	0.476 - 0.495	0.742 - 0.259	1.60 x 1.58	High	32	107	416	690
							Low	123	702	414	1111
		M4	Ocean Color Aerosol	0.540 -0.560	0.742 - 0.259	1.60 x 1.58	High	21	78	362	581.1
							Low	90	667	315	963.2
		I1	Imagery EDR	0.596 - 0.678	0.371 - 0.387	0.80 x 0.789	Single	22	718	119	240.7
		M5	Ocean Color Aerosol	0.661 - 0.680	0.742 - 0.259	1.60 x 1.58	High	10	59	242	366.6
							Low	68	651	360	827.9
		M6	Atmosph. Correct.	0.738 - 0.752	0.742 - 0.776	1.60 x 1.58	Single	9.6	41	199	415.2
		I2	NDVI	0.842 - 0.880	0.371 - 0.387	0.80 x 0.789	Single	25	349	150	304.1
		M7	Ocean Color Aerosol	0.842 - 0.880	0.742 - 0.259	1.60 x 1.58	High	6.4	29	215	519.8
							Low	33.4	349	340	845.6
	S/WMIR	M8	Cloud Particle Size	1.225 - 1.251	0.742 x 0.776	1.60 x 1.58	Single	5.4	165	74	273
		M9	Cirrius/Cloud Cover	1.367 - 1.382	0.742 x 0.776	1.60 x 1.58	Single	6	77.1	83	253
		I3	Binary Snow Map	1.571 - 1.630	0.371 x 0.387	0.80 x 0.789	Single	7.3	72.5	6	172
		M10	Snow Fraction	1.571 - 1.630	0.742 x 0.776	1.60 x 1.58	Single	7.3	71.2	342	714
		M11	Clouds	2.233 - 2.280	0.742 x 0.776	1.60 x 1.58	Single	0.12	31.8	10	25
Emissive Bands		I4	Imagery Clouds	3.549 - 3.936	0.371 x 0.387	0.80 x 0.789	Single	270	353	2.5	0.4
		M12	SST	3.598 - 3.791	0.742 x 0.776	1.60 x 1.58	Single	270	353	0.396	0.13
		M13	SST Fires	3.986 - 4.144	0.742 x 0.259	1.60 x 1.58	High	300	343	0.107	0.04
							Low	380	634	0.423	
	LWIR	M14	Cloud Top Properties	8.406 - 8.747	0.742 x 0.776	1.60 x 1.58	Single	270	336	0.091	0.06
		M15	SST	10.233 - 11.247	0.742 x 0.776	1.60 x 1.58	Single	300	343	0.07	0.03
		I5	Cloud Imagery	10.560 - 12.488	0.371 x 0.387	0.80 x 0.789	Single	210	340	1.5	0.4
		M16	SST	11.402 - 12.316	0.742 x 0.776	1.60 x 1.58	Single	300	340	0.072	0.04

using two point sources to interpolate or extrapolate radiance from count that is converted from electronic voltage. For reflective bands, the VIIRS sensor looks at an onboard solar diffuser and cold space several dozen times for each scan [5]–[8]. The solar diffuse is monitored by the solar diffuser stability monitoring once per day. The VIIRS emissive band calibration concept is also a two-point calibration by viewing onboard blackbody and cold space [1]. However, the VIIRS calibration algorithm is more complicated than other sensors such as AVHRR and MODIS, because of the instrument response verses the scan angle. The thermal emissive bands (TEB) are calibrated using an on-board Calibration Black Body (OBCBB) that has been carefully characterized in prelaunch. The OBCBB emissivity is estimated to be 0.99609–0.99763 for the TEB bands based on prelaunch testing in the thermal vacuum chamber. The OBCBB temperature is carefully controlled using heater elements and thermistors. The calibration algorithm, based on measured BB temperature and emissivity, computes radiances and compares it with counts to determine gain adjustments. Because of emissive background variations caused by the half-angle scanning mirror, and components in the surround including the rotating telescope assembly, half angle mirror (HAM), scan cavity, and shield, additional corrections must be made for this scan-angle dependent response. The characteristics of the VIIRS sensors are carefully measured in prelaunch and stored in look-up tables.

The validation and assessment of the sensor are focused on vicarious calibration, cross-calibration, comparisons with theoretical simulations, and impact studies [9]. McCorkel *et al.* [10] present results of radiometric calibration of Hyperion based on the reflectance-based approach of vicarious calibra-

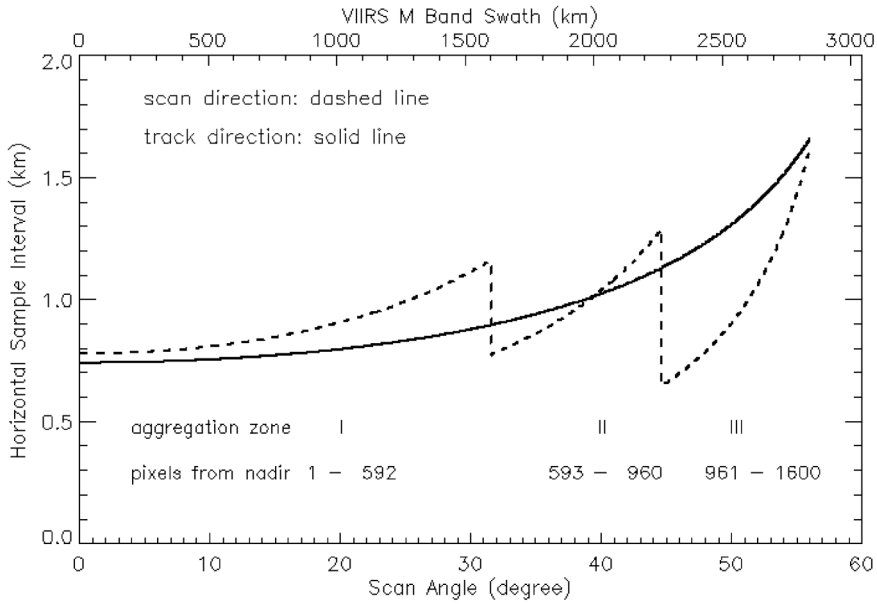

Fig. 1. VIIRS pixel resolution varies with the scan angles. The maximum scan angle is about 56.06° and the maximum zenith angle at the surface is 70°.

tion implemented by University of Arizona during 2001–2005. Vicarious calibration was also applied to the third and fourth Stokes components measurements [11]. There are many cross-calibrations in which two sensors have similar spectral characteristics at collocated locations and time [12], [13]. Comparisons between simulations and measurements can be very valuable [14], [15]. The Monitoring of IR Clear-Sky Radiances over Oceans for sea surface temperature (SST)[1] is a web-based near-real time system developed at National Environmental Satellite, Data, and Information Service (NESDIS) which monitors corresponding Community Radiative Transfer Model (CRTM) Model Minus Observation (M-O) biases (VIIRS BTs associated with SST) and corresponding SST differences over global ocean [16]. For the cross-sensor comparison, radiative transfer calculations are particularly important to take account for the slight difference in spectral bands and sensor viewing directions between two sensors [16]. We have analyzed the VIIRS telemetry data and onboard calibration data to evaluate the instrumental stabilities and performance including signal to noise ratio (SNR) for reflective spectral bands and NEdT for thermal emissive bands. Using the NOAA simultaneous nadir observation (SNO) [17] prediction, we have compared the VIIRS data with MODIS and AVHRR. We have also compared the VIIRS TEB with the CrIS without the SNO limitations since both VIIRS and CrIS are onboard the same platform. This paper is organized as the followings. Section II describes the sensor characteristics and data. The VIIRS thermal emissive band performance is given in Section III. Cross-sensor verification and calibration are given in Section IV. The final Section V is the discussion and summary.

II. Instruments Characteristics and Data Description

VIIRS is an operational sensor to provide moderate-resolution and image resolution data of the globe twice daily without any gap. There is overlapping between orbital data because of its wider scan swath. The M bands have better signal to noise ratio and accuracy which are better suited for quantitative applications, while the imaging bands have a high spatial resolution with broader spectral response. VIIRS does not have infrared atmospheric sounding bands equipped MODIS, since CrIS on the same platform provides 1305 sounding bands.

The VIIRS spectral bands are similar but less than the MODIS. However, seven of the VIIRS bands employ a dual gain technique which makes each of the VIIRS dual gain band to have dual functions. VIIRS uses six dual-gain reflective bands to provide the high radiometric resolution needed for ocean color applications, without saturating the sensor when observing high reflectance surfaces such as land and clouds. The dynamic range of the dual gain bands in high gain is comparable to that of the MODIS ocean color bands, while the dynamic range in the low-gain state is comparable to those of the similar MODIS land bands. The dynamic ranges across all other bands are similar to their MODIS counterparts. VIIRS M13, for example, is used to determine surface temperature at a high gain and forest fire up to a temperature of 683 K at a low gain. The MODIS has to use the band B21 for forest fire up to a temperature of 335 K and the band B22 for normal surface temperatures.

The heritage of the rotating telescope design of VIIRS came from the SeaWiFS's design, which provides better straylight control at high scan angles, while at the same time reduces the response vs. scan angle effects that MODIS has (paddle mirror on MODIS vs. half angle mirror on VIIRS). The MODIS is a two-sided paddle-wheel scanning spectral radiometer. The 360° rotating paddle-mirror is centered with a scan cavity to provide the optical subsystem with sequential views of calibrators and the earth [18]. The larger of the rotating angle, the larger scan angle effect. The higher Suomi NPP and future JPSS orbits (830 km, vs. 705 km for EOS MODIS platforms) allows full global coverage in one day but also requires better straylight control.

[1]MICROS; www.star.nesdis.noaa.gov/sod/sst/micros/

Reflected and emitted radiation from the earth enters the sensor through the Rotating Telescope Assembly (RTA) and is reflected from a rotating Half Angle Mirror (HAM) into a stationary aft-optics subsystem. The light is then spectrally and spatially separated by dichroic beamsplitters and directed to three separate focal plane arrays (FPAs): the Visible/Near Infrared (Vis/NIR) FPA, the Shortwave/Midwave Infrared (SW/MWIR) FPA, and the Longwave Infrared (LWIR) FPA. The light is detected and converted to analog electrical signals in these FPAs and further processed prior to analog-to-digital (A/D) conversion with 12-bit quantization [1]. The digital signals are then processed and multiplexed into the instrument output data stream. Housekeeping data in the form of instrument health, safety, and engineering telemetry are also generated from measurements of internal temperatures, voltages, and currents. These telemetry measurements are reported for every scan.

The DNB is implemented as a dedicated focal plane assembly (FPA) that shares the optics and scan mechanism of the other VIIRS spectral bands [19]. The DNB is a broadband (0.5–0.9 μm) for measuring night lights, reflected solar and/or moon lights over 7 orders of magnitude in dynamic range, which allows the detection of reflected signals from a quarter moon illumination to the brightest daylight. Moonlight is indirect daylight and its magnitude is much smaller than that of daylight. To achieve this large dynamic range it uses a three-stage focal plane: a low-gain stage (LGS) is used to observe daytime scenes, a mid-gain stage (MGS) is used to observe dawn or dusk scenes near the Earth's terminator, and a high-gain stage (HGS) is used to observe nighttime scenes with lunar illumination or late twilight. The HGS is also sensitive to city lights, nighttime fires, fishing boats, lightning and the Aurora Borealis. The sensor maintains a nearly constant 0.75 km resolution over the entire 3000-km swath using an on-board aggregation scheme. This requires 32 aggregation zones across the swath, compensating for perspective and foreshortening, so that the zones near the edge of the swath have the least number of pixels aggregated. Because the aggregating is done on-board, ground calibration must calibrate each aggregation zone separately. The on-board reflective calibration source is a solar diffuser (SD), which is observed once per scan. A space view (SV) is also used for an offset.

VIIRS thermal emissive band (TEB) has two image emissive bands (I4 and I5) and 5 moderate-resolution bands (M12, M13, M14, M15, and M16). The 7 emissive bands are centered at 3.74 (I1), 11.45 (I2), 3.70 (M12), 4.05 (M13), 8.55 (M14), 10.76 (M15), and 12.01 (M16) microns. The two emissive image bands are mainly for cloud imagery and precise geolocation. The 5 moderate-resolution emissive bands are used to determining surface temperature and cloud top pressure. The only dual gain band TEB M13 is used for determining surface temperature at low radiance, and fire detection at high radiance.

The VIIRS data are divided into three levels: the Raw Data Records (RDRs or level 0), Sensor Data Records (SDRs or level 1), and Environmental Data Records (EDRs or level 2). The RDR data contain engineering and house-keeping data for spacecraft and sensor monitoring, and science data for SDR production. The SDR data are calibrated radiance/reflectance and brightness temperatures with geolocation. The SDR data are the inputs to EDRs algorithms for such applications as cloud and aerosol properties, ocean color, sea and land surface temperature, ice temperature, fires, and Earth's albedo. Climatologists will also use VIIRS data to improve our understanding of global climate change.

The VIIRS data are stored in Hierarchical Data Format 5 (HDF5), which is based on a data model and a set of libraries. The HDF5 standardization makes it useful for many disciplines. The standard also allows for flexible temporal aggregation, with granules appended by extending the dataset dimension. Following subsections a) and b) are the adopted data description of Raw Data Records and Sensor Data Records [1]:

a) Raw data records (RDR): The NPP RDR is an accumulation of binary data generated by sensors on board the NPP spacecraft and is assembled into groups called application packets (APs). Unique Application Packet Identifier (APID) numbers represent each discrete AP type. The NPP ground processing software collects one or more groups of related APs together into granules which are then assembled into common RDR structures and combined with metadata to create the delivered HDF5 file. The APs are accumulated per discrete period and a granule refers to the data accumulated and organized for that discrete period. The APs are logically grouped into science, diagnostic, dwell, dump, and telemetry RDRs. A science RDR data product generally contains all the necessary APs to construct a Science Data Record (SDR). Diagnostic, dwell, and dump RDRs generally contain APs that are only generated while the sensor is in diagnostic mode. Telemetry RDRs generally contain APs that describe the health and status of the sensor.

The required inputs for generating SDR products are the verified VIIRS Raw Data Records (RDRs), which contain the basic digital numbers (DNs) from all viewing sectors to be converted into calibrated top of atmosphere (TOA) radiance, reflectance, and brightness temperature, as well as engineering, health and safety data, and onboard calibrator-view data that are required by the radiometric calibration algorithm. These data have been unpacked from VIIRS RDR packets in standard Consultative Committee for Space Data System (CCSDS) format, and assembled into scan cube structures. As part of the unpacking these data are uncompressed, band identified, and quality checked through a re-computation of embedded checksums.

The VIIRS provides seven types of RDRs in CCSDS packet format. They are: Memory Dump, High Rate Data (HRD), Housekeeping Telemetry, Engineering Launch, Early Orbit and Activation (LEO&A), Calibration Time of Day and Ephemeris.

In the process of verifying the RDR data, quality flags, triggered by missing or corrupted data, are included along with the Earth-view counts, the space-view counts, the OBCBB and the solar diffuser-view counts. If any of these are flagged as bad, this quality flag is passed through to the SDR output quality flag for each pixel. In the cases of calibrator quality flags, a bad detector in the calibrator causes a bad quality flag to be set for the entire scan or scans that use that calibration data. Details on the structure and contents of the VIIRS RDRs can be found from the common data format control documents at: http://www.star.nesdis.noaa.gov/jpss/.

TABLE II
VIIRS THERMAL EMISSIVE BAND SPECIFICATION, PRELAUNCH, AND ON-ORBIT PERFORMANCE

VIIRS Bands	Central wave-length (μm)	Ttyp for Specification (K)	Dynamic Limits (K)		NeDT (K)		
			Low	High	Specifi-cation	Pre-launch	On-orbit Adjusted to Ttyp
I4	3.74	270	208	367	2.5	0.4	0.4
I5	11.45	210	150	380	1.5	0.4	0.4
M12	3.70	270	203	368	0.396	0.13	0.13
M13	4.05	300 (H gain)	192	343	0.107	0.04	0.042
M13	4.05	380 (L gain)	343	683	0.423		< 0.4
M14	8.55	270	120	365	0.091	0.06	0.06
M15	10.76	300	111	381	0.07	0.03	0.03
M16	11.51	300	103	382	0.072	0.04	0.03

b) Sensor data records (SDR): SDRs (or Level 1b) are the calibrated and geolocated radiance and reflectance data produced based on the RDRs in the data processing. There are 22 VIIRS SDRs: 16 moderate-resolution, narrow-spectral-band products, made up of 11 reflective solar bands (RSBs) and 5 thermal emissive bands (TEBs); five imaging-resolution, narrow-spectral-band products, made up of 3 RSBs and 2 TEBs; and 1 DNB imaging broadband product. These SDRs are then used to produce the EDRs.

An SDR contains the following elements: Calibrated sensor data, Geolocation data (where applicable), Quality flags, Metadata at the granule and aggregation level.

Within HDF5, processed VIIRS data for NPP are organized and described by the Unified Modeling Language (UML). This standard modeling language is used to design structured or object-oriented software applications, and provides a uniform means of data retrieval for further use, thus lowering development costs. Details of NPP M-, I-, and Day-Night Band SDR HDF5 data format and content can be found in *Appendix A: SDR Data Contents and Related Information*. Complete details on the VIIRS SDR formats is available from the common data format control documents at: http://www.star.nesdis.noaa.gov/jpss/.

There are three types of VIIRS SDRs: Calibrated top-of-atmosphere (TOA) Radiances, Calibrated TOA Reflectance for the RSB bands, Calibrated TOA Brightness Temperature for the TEB bands.

III. VIIRS TEB PERFORMANCE

During the early orbit checkout, VIIRS SDR team detected a decrease in sensor sensitivity on VIIRS I2 and M7 bands. This degradation was not expected and the activation of other channels and instruments was postponed to investigate this issue. Using VIIRS mirror wetness samples, VIIRS SDR team identified a build-up of Tungsten Oxides on the surface of the mirrors that are an essential part of the optical components in VIIRS. These substances cause the mirrors to darken and have an effect on the instrument's behavior when UV radiation strikes the mirror. Fortunately, the mirror darkening has negligible effects on the VIIRS thermal emissive bands. A non-standard process during mirror coating was discovered as a potential root cause of the contamination of the mirrors (http://www.spaceflight101.com/npp-mission-updates.html). A routinely updated F and H tables have to be used to take account for the degradation due to the tungsten oxide contamination. A theoretical model was also developed based on the absorption spectrum of the wetness sample mirror. Based on the model prediction, VIIRS projected performance still meets the specification within designed lifetime.

VIIRS Cryo-cooler door was opened and thermal emissive band measurement was taken on Jan. 18, 2012. There were problems on incorrect look-up tables, code bugs, and incomplete flags. After those issues are fixed, NASA, AeroSpace, and NOAA VIIRS SDR teams have obtained the similar results. The VIIRS sensor stability is important to operational satellite products. We have monitored the instrumental telemetry variables and radiometric performance. The monitored telemetry variables are: controller voltages, motor currents, thermistor resistor, and instrumental temperatures. In order to reduce instrumental noise, the temperature for the long-wave and mid-wave focal planes is controlled under 80 K. The VIIRS TEB radiometric performance meets the specification (see Table II). The dynamic range of the brightness temperature in the specification is within operational dynamic limits. Note that the M13 calibration at the low gain cannot be evaluated at real time, and it wasn't evaluated at prelaunch. M13 NeDT at a low gain in Table II was estimated using the VIIRS blackbody warm-up and cool-down in February, 2012.

For a given detector, NeDT is very stable. We can calculate the M13 NeDT at a high gain (HG), but we cannot calculate the M13 NeDT at a low gain (LG) at real time. The low gain mode of the VIIRS band M13 is intended for fire detection, and consequentially has a very high limit of 683 K. This creates problems in using the OBCBB for calibration, because at its nominal temperature of 292.5 K there are only about 4 counts detected per sample. This produces a very low signal to noise ratio of 6.5, and unfortunately aggregation does not improve it, because the error is not random but is fixed. Therefore, samples averaging don't improve the SNR. There is a challenge for the VIIRS M13 band calibration at the low gain. The Blackbody temperature is far below the lowest temperature (343 K) of low gain, which prevents from onboard calibration. At the present, the calibration at low gain relies on pre-launch calibration coefficients, c_0 and c_1 (offset and slope). There are the VIIRS M13 Moon measurements with a sequence of two scans at the low gain and followed by two scans at the high gain. By assuming the same moon temperatures for the adjacent two scans at LG and two scans at HG, one may collocate

TABLE III
M13 CALIBRATION COEFFICIENTS AT THE LOW GAIN

	c_1	c_0	Description
1	0.1320±0.0020	1.15±0.015	Prelaunch for BT < 634 K
2	0.1420±0.0003	-0.006±0.007	M13 HG radiances and LG counts are matched spatially over SV moon observations.
3	0.1412±0.0030	0	Using BB calibration data at 315 K during the BB warm-up and cold down

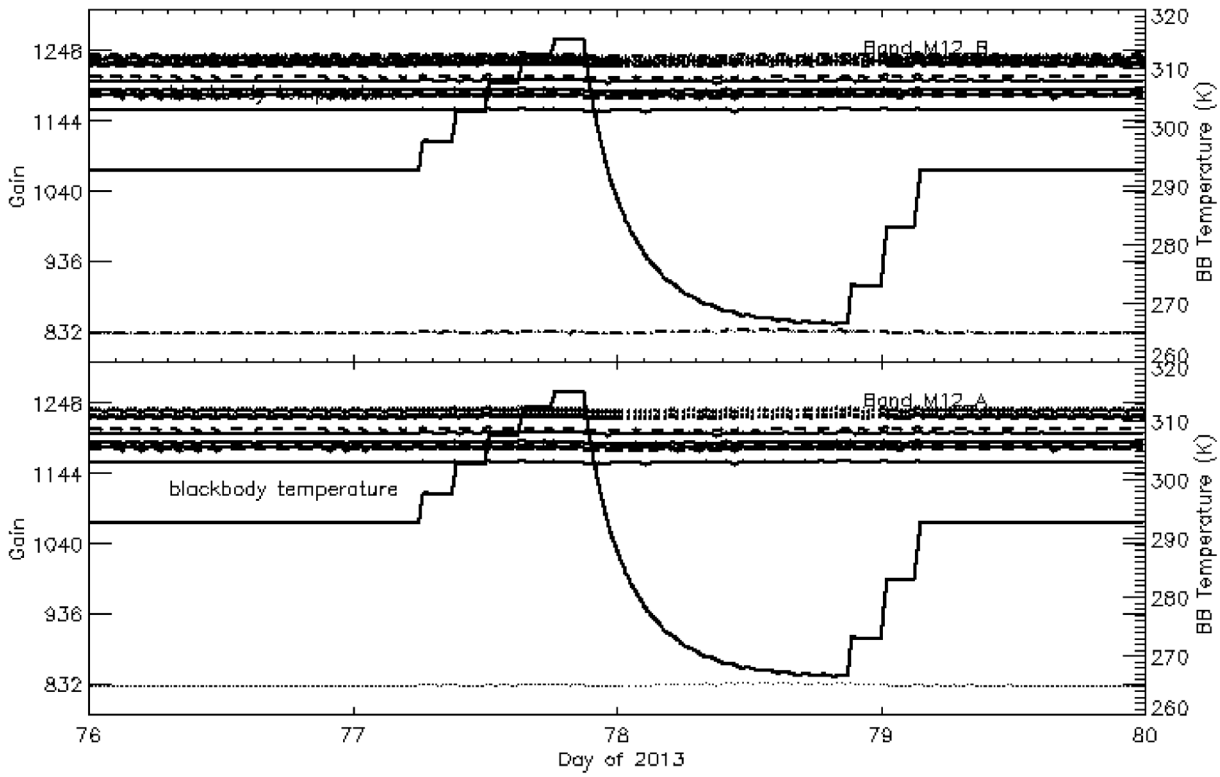

Fig. 2. M12 gain varies with time. The solid black line represents BB temperature (see y-axis at the right). Different symbols and line styles correspond to different detectors.

HG radiance with LG count. McIntire *et al.* [20] at the NASA calculated the M13 low-gain coefficients by using M13 radiance at the high-gain and counts at the low-gain. We at the NOAA have derived the M13 LG coefficients using blackbody (BB) warm-up and cool-down calibration data [21]. NASA's and NOAA's approaches obtained almost the same calibration coefficients which indicate the BB warm-up and cool-down data are useful to determine the M13 LG calibration coefficients and NEdT. The onboard M13 gain at LG is about 7% larger than prelaunch value that is used in the current calibration. Table III summarized the prelaunch, NASA's, and NOAA's calibration coefficients for the VIIRS M13 at the low gain stage.

We have analyzed gains, NeDN, and NeDT for each detector, each half-mirror side (A or B), and each gain stage. All TEB have a single gain, except for M13. The gain is the mean account of the blackbody divided by radiance, the Planck function at the blackbody temperature. Since the detector response is approximately linear, therefore the gain for a given band should be constant for a given detector and a HAM side. Fig. 2 showed that the M12 gain varies with time during a BB warm-up and cool-down between March 17 and 20, 2013. The gain is almost constant which implies that the detector has a linear response. The line in the bottom is the gain for detector #16. Obviously, the response of detector #16 is about 30% lower than others, which can cause a larger NeDT.

Fig. 3 showed that I4 gain change with time. It can be seen from the figure that the gain depends slightly on the BB temperature and the non-linearity needs to be considered. We analyzed all VIIRS TEB data during the warm-up and cool-down. It is found that M14 gain has the largest non-linearity effect.

NeDN is the sensor noise in radiance. It is an internal noise of the instrument, ideally independent from the blackbody view, space view, and the Erath view. As shown in Fig. 4, I4 NeDN doesn't significantly change with time. However, for the same noise, NeDT changes with the target temperature because of the non-linearity between Planck radiance and brightness temperature. As shown by Fig. 5, the NeDT decreases as the brightness temperature increases. In all numerical weather prediction (NWP) centers, microwave and infrared brightness temperatures are used because brightness temperature is equivalent to a temperature of a blackbody. For an infrared window band, the brightness temperature can be directly used

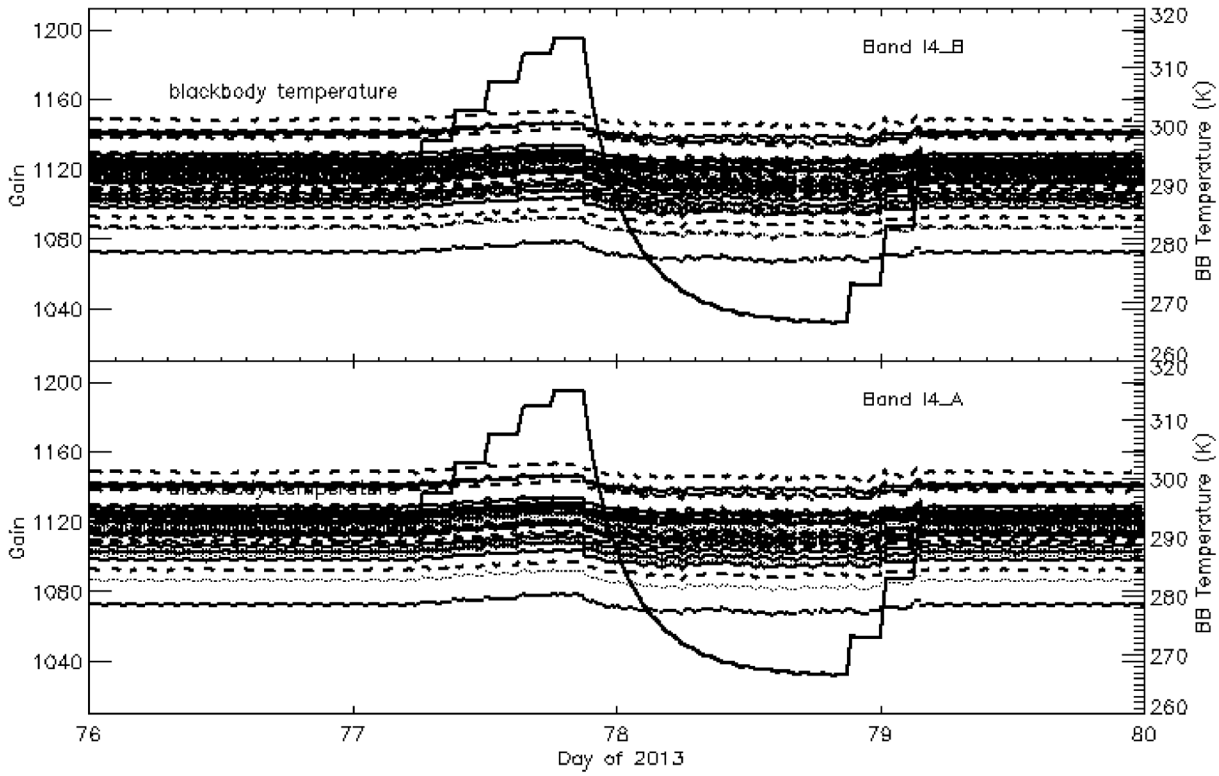

Fig. 3. Same as Fig. 2, but for I4.

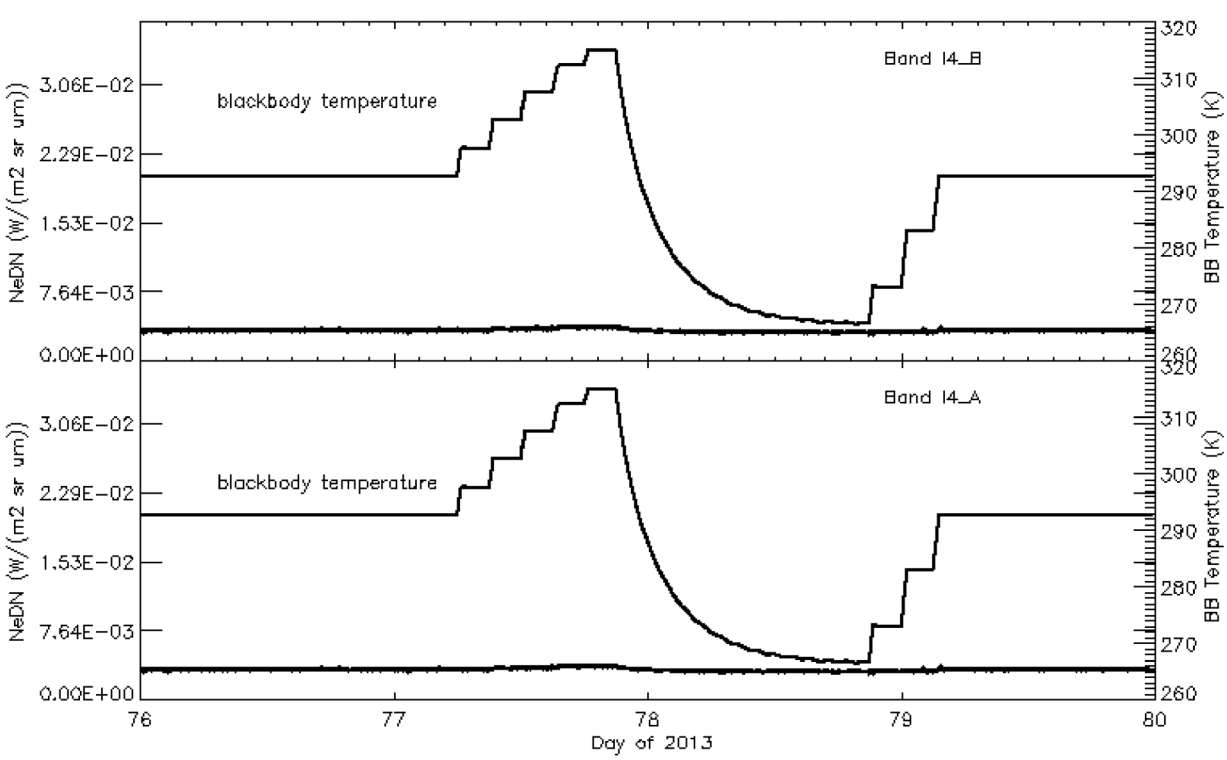

Fig. 4. I4 NeDN varies with time. The solid black line represents BB temperature (see y-axis at the right). Different symbols and line styles correspond to different detectors.

to estimate a sea surface temperature by removing atmospheric effect. However, the NWP centers use static instrument NeDT. It is worthy to be emphasized that various instrument NeDT need to be used.

We have also monitored a long time series of blackbody counts and space view counts for the VIIRS TEB. The result showed that the VIIRS TEB is stable except for few spikes due to bad data.

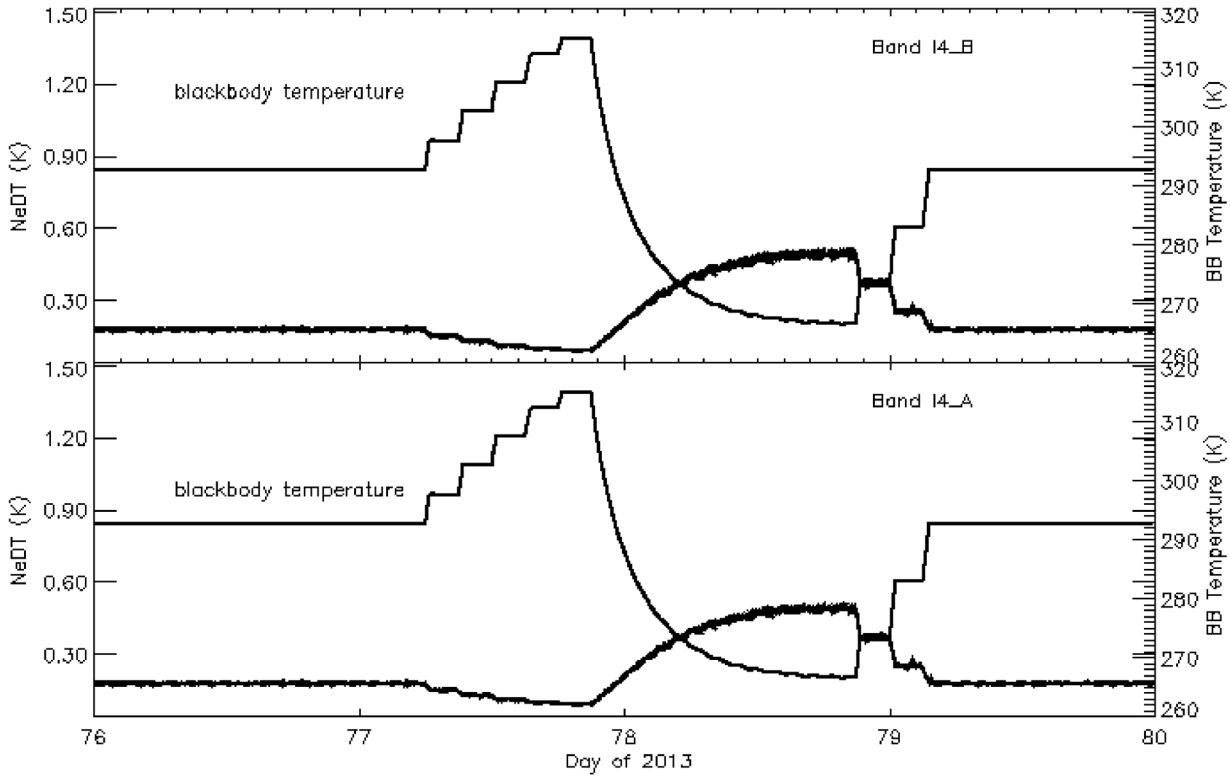

Fig. 5. I4 NeDT varies with time. The solid black line represents BB temperature (see y-axis at the right). Different symbols and line styles correspond to different detectors.

TABLE IV
VIIRS, MODIS, AVHRR, AND CRIS CHANNELS FOR CROSS-SENSOR VALIDATION

VIIRS (μm)	MODIS (μm)	AVHRR (μm)	CrIS (μm)
I4 (3.549 - 3.936) M12 (3.598 - 3.791)	B20 (3.660 - 3.840)	A3B (3.53 – 3.93)	
M13 (3.986 – 4.144)	B23 (4.020 - 4.080)		SW (129 channels) (3.92-4.64)
M14 (8.406 – 8.747)	B29 (8.400 - 8.700)		
M15 (10.233-11.247) M16 (11.402-12.316) I5 (10.560 - 12.488)	B31 (10.78 - 11.28) B32 (11.77 - 12. 27)	A4 (10.30 – 11.30) A5 (11.50 – 12.50)	LW (713 channels) (9.13-15.38)
			MW (433 channels) (5.71 – 8.28)

IV. Comparisons With AVHRR, MODIS, and Cris Sensor

From the results of gain, NeDT, and NeDN for long-term monitoring system and the results during blackbody temperature warm-up and cool-down (see Figs. 2–5), we showed that the VIIRS TEB is stable and meets the specification in the above section. This section will demonstrate the consistency among sensors, from a view of application. For applications, users need the consistent measurements for satellite products and climate studies. We used the NOAA simultaneous nadir observation (SNO) prediction [22] to collect the VIIRS and AVHRR data, the VIIRS and MODIS data [23]. NOAA/NESDIS Center for Satellite Applications and Research (STAR) has developed a SNO algorithm and operationally applied for the NOAA operational satellites and other satellite including MODIS. The SNO technique allows us to analyze the bias and standard deviation between the VIIRS and other measurements over homogenous scenes, for example oceans (warm target) and over DomeC (cold target) in Antarctic. We spectrally match the comparison data set: VIIRS (I band and M band) vs AVHRR (A band), VIIRS vs MODIS (B band), and VIIRS vs CrIS. Fig. 6 plotted the VIIRS, AVHRR, MODIS relative spectral response functions and a CrIS measured brightness temperature for a clear-sky case. CrIS is a hyper spectral sensor and the hyper spectral data can be convoluted with the VIIRS' spectral response function to simulate the VIIRS band radiance and brightness temperature. M15 and M16 are covered by the CrIS. M12 and M13 are partially outside the CrIS spectra. M14 locates at the gap of the CrIS data. Since both the VIIRS and CrIS on the

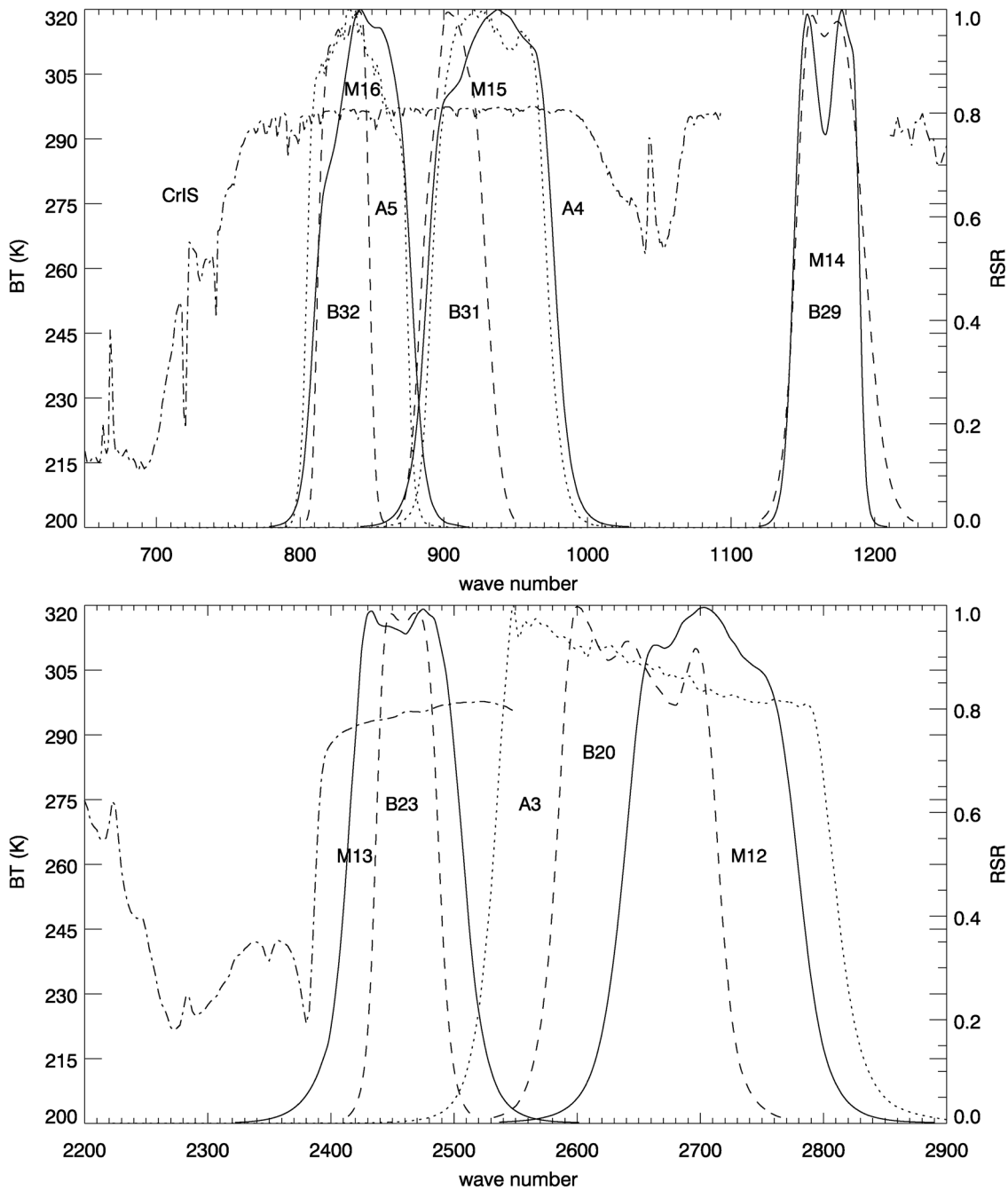

Fig. 6. VIIRS M bands (solid lines), MODIS (B bands, dashed lines), AVHRR (A bands, dotted lines) relative spectral response function and a CrIS measured brightness temperature (dash-dotted lines) for a clear-sky case.

same platform of the NPP, the collocation is straightforward. AVHRR channel 4 (A4) and channel 5 (A5) match the M15 and M16, respectively. MODIS band B31 and B32 are comparable to the M15 and M16 respectively. Table IV lists their channels for this comparison. The VIIRS, the MODIS, and the AVHRR data are averaged over a grid of 0.25 by 0.25 degrees, individually. Data are selected when the standard deviation of the brightness temperature in each grid is less than 0.6 K.

From Fig. 6 one can see that VIIRS M15 and AVHRR channel 4 agree well in the sensor response data. So agree VIIRS M16 and AVHRR channel 5 spectral response data. VIIRS I4 and AVHRR channel 3 spectrally agree, too (I band spectral response data are not shown in Fig. 6). We use the NOAA SNO prediction data to select match-up VIIRS and AVHRR observations. The VIIRS and the AVHRR data were matched into gridded data. Each grid represents 0.25 by 0.25 degrees in latitude and longitude. Fig. 7 showed a comparison between AVHRR for A4 and A5 and VIIRS for M15 and M16 at about 13:45 March 04, 2012, individually. The two sensors agree well with a standard deviation of 0.2 K and a bias of 0.3 K. The standard deviation reflects instrumental noise. The main part in bias is due to the small difference in spectral responses of the two sensors and zenith angles. We applied the Community Radiative Transfer Model (CRTM) [24] and

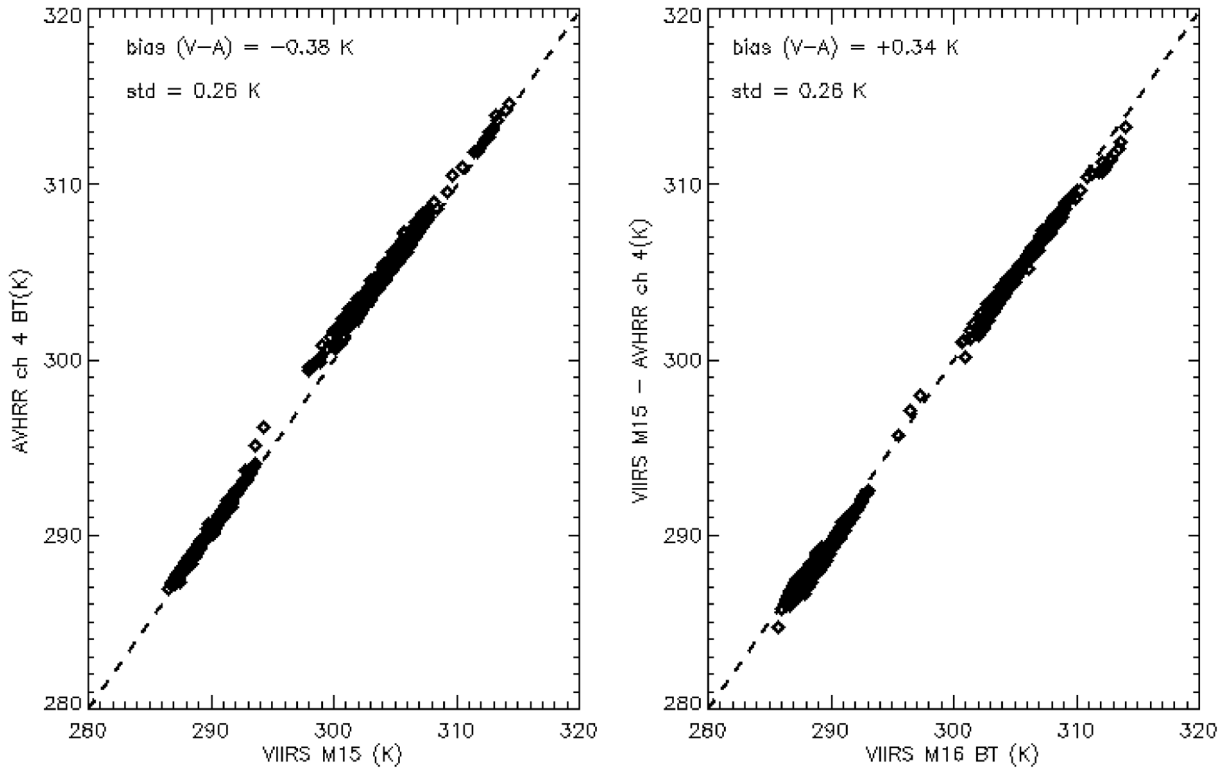

Fig. 7. Comparisons between AVHRR (A4, A5) and VIIRS (M15, M16) from 13:43 and 13:49 UTC, March 04, 2012. Only pixels with a zenith angle less than 5° over desert are used here.

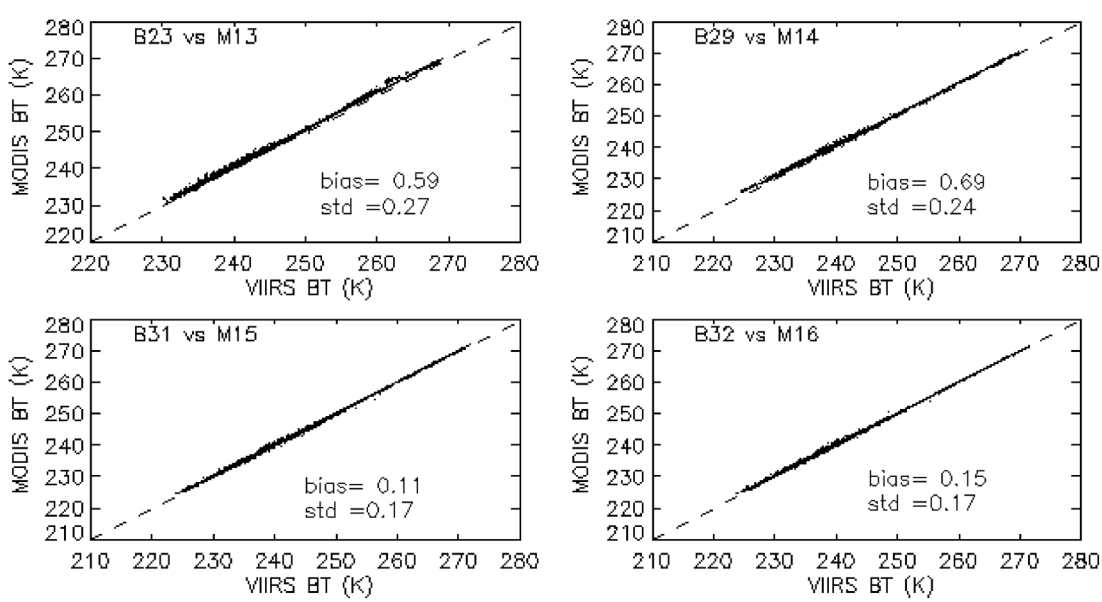

Fig. 8. Comparisons between VIIRS and MODIS on March 18, 2012. Both VIIRS and MODIS data are averaged over 0.25° grids in latitude and longitude.

use the European Centre for Medium-Range Weather Forecast (ECMWF) analysis data to simulate the VIIRS radiance at the VIIRS's zenith angle and the AVHRR radiance at the AVHRR's zenith angles. We compute the difference between the VIIRS (AVHRR) measurement and the VIIRS (AVHRR) CRTM simulation. The double difference ((VIIRS measurement–VIIRS simulation)–(AVHRR measurement–AVHRR simulation)) is less than 0.1 K, smaller than the original bias between the VIIRS and AVHRR measurements.

Using the SNO technique, we also compared MODIS and VIIRS over DomeC on Feb. 25, 2012. We have performed the comparison for 4 sets: B23 vs M13, B29 vs M14, B31 vs M15, B32 vs M16. None of their response functions are the same, but they are close. Fig. 8 shows the comparisons between 4 VIIRS bands and 4 MODIS bands, respectively. Slight bias is expected because of the spectral response difference between VIIRS and MODIS. We also analyzed the bias between VIIRS M12 and the MODIS B20. The large bias (∼2 K) for M12 at daytime is due

to the difference in reflected solar radiation at different spectral response of the two sensors.

The last comparison was carried out between the VIIRS and CrIS. Both sensors are onboard the same platform, so that we can compare them at any time and any location. However, average of multiple VIIRS pixels doesn't fill out whole CrIS pixel, therefore we select homogeneous scenes determined by the VIIRS pixels. Both VIIRS and CrIS share the same geolocation algorithm, which enables us to precisely collocate measurements from the two sensors. The VIIRS data will be averaged over the CrIS pixel. The high-spectral CrIS data can create the VIIRS-like band radiance by the convolution of the CrIS radiance with the VIIRS relative spectral response (RSR) data. There is a gap in the CrIS spectral data and M12, M14 and I4 are not covered by the CrIS. Results showed that both CrIS and VIIRS for M15 and 16 agree within 0.5 K. By closely look at the VIIRS and CrIS comparison, CrIS SDR team found a scene temperature dependent bias and a large bias $(\mathrm{VIIRS\ M15} - \mathrm{CrIS} = -0.4\ \mathrm{K})$ was seen at a low scene temperature of 200 K. We are going to use Community Radiative Transfer Model (CRTM) [24], [25], developed at the Joint Center for Satellite Data Assimilation in the United States, to investigate the bias and root cause.

V. Discussion and Summary

VIIRS significantly outperforms the legacy AVHRR in spatial, spectral, and radiometric accuracy. Early assessment of the VIIRS TEB calibration shows that VIIRS TEB is stable and meets the specification. The onboard calibration accuracy for NeDT very consists with pre-launch thermal vacuum tests. Consistency test among VIIRS, MODIS, AVHRR, and CrIS further confirms the stability and accuracy of the VIIRS TEB. The VIIRS thermal emissive bands have been using for the surface temperature and cloud mask products.

However, there are reminded issues that need to be investigated. For M13 at a low gain, we cannot perform analysis of calibration accuracy and uncertainty at real time. Generally, the VIIRS TEB is stable and occasional assessment of the M13 at LG may be sufficient for fire detection purpose. As summarized in Table III, both NASA's result using moon measurements and NOAA's calibration coefficients derived from the data for blackbody warm-up and cool-down suggested that the prelaunch calibration slope coefficient was underestimated by 7%.

The large bias between VIIRS M15 and CrIS at low temperatures is under investigation. We studied the M15 gain and NeDN. M15 NeDN doesn't change as the blackbody temperature changes. The gain changes with the blackbody temperature, which implies the importance of non-linearity. The nonlinearity for the CrIS calibration can be significant, too. The CrIS prelaunch data shows that without non-linear correction term, the long-wave band brightness temperature may be overestimated up to 0.5 K at a temperature of 233 K.

We observed the small periodic change of the 3rd and 6th PRTs. It shows that the periodic change of the two PRTs is coincident with solar zenith angle at the Earth surface. The root cause of the PRTs' periodic change is not identified yet.

As shown in Fig. 5, NeDT depends on scene temperatures. It is worthy to be pointed out that such a dependence needs to be included in the measurement error if brightness temperature is used. For a given sensor, the scene temperature dependent NeDT can be derived as long as its gain and NeDN are nearly constant.

The VIIRS data user community reported the M12 image striping at daytime. The striping in the along-track direction displays a periodic pattern comes from the fact that VIIRS uses 16 detectors for each M band and 32 detectors for each I band. The striping wasn't observed at nighttimes. It was found that the residual striping was caused by the significant difference among the 16 detector's azimuth angles.

Overall, the VIIRS TEB is in good quality for applications.

References

[1] *"Visible/Infrared Imager Radiometer Suite (VIIRS) Sensor Data Record (SDR), User's Guide, ver. 1,"* C. Cao, J. Xiong, F. DeLuccia, Q. Liu, S. Blonski, and D. Progorzala, Eds., National Oceanic and Atmospheric Administration (NOAA), 2011.

[2] C. Cao, X. Xiong, A. Wu, and X. Wu, "Assessing the consistency of AVHRR and MODIS L1B reflectance for generating fundamental climate data records," *J. Geophys. Res.*, vol. 113, p. D09114, 2008, 10.1029/2007JD009363.

[3] H. Oudrari, J. McIntire, D. Moyer, K. Chiang, X. Xiong, and J. Butler, "Preliminary assessment of Suomi-NPP VIIRS on-orbit radiometric performance," *Proc. SPIE 8510, Earth Observing Systems XVII, 851011*, Oct. 15, 2012, 10.1117/12.930498.

[4] R. E. Wolfe, G. Lin, M. Nishihama, K. P. Tewari, and E. Montano, "NPP VIIRS early on-orbit geometric performance," *Proc. SPIE 8510, Earth Observing Systems XVII, 851013*, Oct. 15, 2012, 10.1117/12.929925.

[5] J. P. Fulbright, N. Lei, K. Chiang, and X. Xiong, "Characterization and performance of the Suomi-NPP/VIIRS solar diffuser stability monitor," *Proc. SPIE 8510, Earth Observing Systems XVII, 851015*, Oct. 15, 2012, 10.1117/12.930494.

[6] Lee, J. McIntire, and H. Oudrari, "Characterization of Suomi-NPP VIIRS reflective solar bands dual gain anomaly," *Proc. SPIE 8510, Earth Observing Systems XVII, 851017*, Oct. 15, 2012, 10.1117/12.930468.

[7] N. Lei, Z. Wang, J. Fulbright, S. Lee, J. McIntire, K. Chiang, and X. Xiong, "Initial on-orbit radiometric calibration of the Suomi NPP VIIRS reflective solar bands," *Proc. SPIE 8510, Earth Observing Systems XVII, 851018*, Oct. 15, 2012, 10.1117/12.930486.

[8] F. De Luccia, D. Moyer, E. Johnson, K. Rausch, N. Lei, K. Chiang, X. Xiong, J. Fulbright, E. Haas, and G. G. Iona, "Discovery and characterization of on-orbit degradation of the Visible Infrared Imaging Radiometer Suite (VIIRS) Rotating Telescope Assembly (RTA)," *Proc. SPIE 8510, Earth Observing Systems XVII, 85101A*, Oct. 15, 2012, 10.1117/12.930544.

[9] A. Baraldi, "Impact of radiometric calibration and specifications of spaceborne optical imaging sensors on the development of operational automatic remote sensing image understanding systems," *IEEE J. Sel. Topics Appl. Earth Observ. Remote Sens.*, vol. 2, pp. 104–134, 2009.

[10] J. McCorkel, K. Thome, and L. Ong, "Vicarious calibration of EO-1 Hyperion," *IEEE J. Sel. Topics Appl. Earth Observ. Remote Sens.*, vol. 6, no. 2, pt. 1, pp. 400–407, Apr. 2013, 10.1109/JSTARS.2012.2225417.

[11] Q. Liu and F. Weng, "Vicarious calibration of the third and fourth Stokes parameters of Windsat measurements," *Appl. Opt.*, vol. 44, pp. 7403–7406, 2005, 2005.

[12] N. Yokoya, N. Mayumi, and A. Iwasaki, "Cross-calibration for data fusion of EO-1/Hyperion and Terra/ASTER," *IEEE J. Sel. Topics Appl. Earth Observ. Remote Sens.*, vol. 6, no. 2, pt. 1, pp. 419–426, Apr. 2013, 10.1109/JSTARS.2012.2208449.

[13] A. Wu, Y. Xie, X. Xiong, and I. Chu, "Assess calibration consistency of MODIS and AVHRR thermal Infrared bands using SNO observations corrected for atmospheric effects," *IEEE Geosci. Remote Sens. Lett.*, vol. 9, no. 3, pp. 487–491, 2012.

[14] K. Segl, L. Guanter, C. Rogass, T. Kuester, S. Roessner, H. Kaufmann, B. Sang, V. Mogulsky, and S. Hofer, "EeteS—The EnMAP end-to-end simulation tool," *IEEE J. Sel. Topics Appl. Earth Observ. Remote Sens.*, vol. 5, pp. 522–530, 2012.

[15] F. Li, D. L. B. Jupp, S. Reddy, L. Lymburner, N. Mueller, P. Tan, and A. Islam, "An evaluation of the use of atmospheric and BRDF correction to standardize Landsat data," *IEEE J. Sel. Topics Appl. Earth Observ. Remote Sens.*, vol. 3, pp. 257–270, 2010.

[16] X. Liang and A. Ignatov, "Monitoring of IR clear-sky radiances over oceans for SST (MICROS)," *JTech*, vol. 28, 2011, 10.1175/JTECH-D-10-05023.1.

[17] A. Wu and X. Xiong, "NPP VIIRS and aqua MODIS RSB comparison using observations from simultaneous nadir overpasses (SNO)," *Proc. SPIE 8510, Earth Observing Systems XVII, 85100P*, Oct. 15, 2012, 10.1117/12.931011.

[18] C. F. Schueler and W. L. Barnes, "Next-generation MODIS for polar operational environmental satellites," *J. Atmos. Oceanic Technol.*, vol. 15, pp. 430–439, 1998.

[19] S. D. Miller, C. L. Combs, S. Q. Kidder, and T. F. Lee, "Assessing moonlight availability for nighttime environmental applications by low-light visible polar-orbiting satellite sensors," *J. Atmosph. Ocean. Technol.*, vol. 29, no. 4, pp. 538–557, 2012.

[20] J. McIntire, B. Efremova, and X. Xiong, "Calibration of NPP VIIRS fire detection band using lunar observations," *Proc. SPIE 8533, Sensors, Systems, Next-Generation Satellites XVI, 85331B* Nov. 19, 2012, http://dx.doi.org/10.1117/12.971228.

[21] Q. Liu, K. Chiang, C. Cao, J. Xiong, X. Shao, S. Blonski, and F. Weng, "Calibration of low gain radiance at VIIRS emissive band (M13) and VIIRS image about moon temperature," *Proc. SPIE 8528, Earth Observing Missions and Sensors: Development, Implementation, Characterization II, 85280O* Nov. 19, 2012, http://dx.doi.org/10.1117/12.97970.

[22] C. M. Cao, M. M. Weinreb, and H. Xu, "Predicting simultaneous nadir overpasses among polar-orbiting meteorological satellites for the intersatellite calibration of radiometers," *J. Atmos. Oceanic Technol.*, vol. 21, pp. 537–542, 2004.

[23] T. Chang and X. Xiong, "Assessment of MODIS thermal emissive band on-orbit calibration," *IEEE Trans. Geosci. Remote Sens.*, vol. 49, no. 6, pp. 2415–2425, 2011.

[24] F. Weng and Q. Liu, "Satellite data assimilation in numerical weather prediction models, Part I: Forward radiative transfer and jocobian modeling in cloudy atmospheres," *J. Atmos. Sci.*, vol. 60, pp. 2633–2646, 2003.

[25] Q. Liu and F. Weng, "Advanced doubling-adding method for radiative transfer in planetary atmosphere," *J. Atmos. Sci.*, vol. 63, pp. 3459–3465, 2006.

Quanhua (Mark) Liu receive the B.S. degree from the Nanjing Institute of Meteorology, Nanjing, China, in 1981, the Master's degree in physics from the Chinese Academy of Science, Beijing, China, in 1984, and the Ph.D. degree in marine science from the University of Kiel, Kiel, Germany, in 1991.

He is with the Joint Center for Satellite Data Assimilation. His primary interests are radiative transfer theory, retrieval methodology, and applications of satellite data.

Changyong Cao is a research physical scientist specializing in the calibration of radiometers onboard NOAA's operational environmental satellites. In addition to the operational pre- and post-calibration support, he is responsible for developing and refining the methodology for inter-satellite calibration using the Simultaneous Nadir Overpass (SNO) method, which has been used for the long-term on-orbit instrument performance monitoring of all radiometers on NOAA's polar orbiting satellites, and is being used by scientists for quantifying inter-satellite calibration biases in developing long-term time series for climate change detection studies. His primary research interest is climate quality calibration for earth observing satellites. He is co-chair of the Calibration Product Oversight Panel (CalPOP), and the chair for the GOES-R calibration working group. He also chaired the CEOS/WGCV (Committee on Earth Observation Satellites/Working Group on Calibration/Validation), the international committee for all space agencies from 2007 to 2008.

Fuzhong Weng received the Master degree in radar meteorology from the Nanjing Institute of Meteorology, Nanjing, China, in 1985 and the Ph.D. degree from Colorado State University, Fort Collins, CO, USA, in 1992.

He is currently with NOAA/NESDIS/STAR, Camp Springs, MD, USA. He is a leading expert in developing various NOAA operational satellite microwave products and algorithms such as Special Sensor Microwave Imager and Advanced Microwave Sounding Unit cloud and precipitation algorithms, land surface temperature, and emissivity algorithms. He is developing new innovative techniques to advance uses of satellite measurements under cloudy and precipitation areas in numerical weather prediction models.